

Measurement of the rate of $\nu_e + d \rightarrow p + p + e^-$ interactions produced by ^8B solar neutrinos at the Sudbury Neutrino Observatory

Q.R. Ahmad¹⁵, R.C. Allen¹¹, T.C. Andersen¹², J.D. Anglin⁷, G. Bühler¹¹, J.C. Barton^{13†}, E.W. Beier¹⁴, M. Bercovitch⁷, J. Bigu⁴, S. Biller¹³, R.A. Black¹³, I. Blevins³, R.J. Boardman¹³, J. Boger², E. Bonvin⁹, M.G. Boulay⁹, M.G. Bowler¹³, T.J. Bowles⁶, S.J. Brice^{6,13}, M.C. Browne¹⁵, T.V. Bullard¹⁵, T.H. Burritt^{15,6}, K. Cameron¹², J. Cameron¹³, Y.D. Chan⁵, M. Chen⁹, H.H. Chen^{11*}, X. Chen^{5,13}, M.C. Chon¹², B.T. Cleveland¹³, E.T.H. Clifford^{9,1}, J.H.M. Cowan⁴, D.F. Cowen¹⁴, G.A. Cox¹⁵, Y. Dai⁹, X. Dai¹³, F. Dalnoki-Veress³, W.F. Davidson⁷, P.J. Doe^{15,11,6}, G. Doucas¹³, M.R. Dragowsky^{6,5}, C.A. Duba¹⁵, F.A. Duncan⁹, J. Dunmore¹³, E.D. Earle^{9,1}, S.R. Elliott^{15,6}, H.C. Evans⁹, G.T. Ewan⁹, J. Farine³, H. Fergani¹³, A.P. Ferraris¹³, R.J. Ford⁹, M.M. Fowler⁶, K. Frame¹³, E.D. Frank¹⁴, W. Frat¹⁴, J.V. Germani^{15,6}, S. Gil¹⁰, A. Goldschmidt⁶, D.R. Grant³, R.L. Hahn², A.L. Hallin⁹, E.D. Hallman⁴, A. Hamer^{6,9}, A.A. Hamian¹⁵, R.U. Haq⁴, C.K. Hargrove³, P.J. Harvey⁹, R. Hazama¹⁵, R. Heaton⁹, K.M. Heeger¹⁵, W.J. Heintzelman¹⁴, J. Heise¹⁰, R.L. Helmer^{10†}, J.D. Hepburn^{9,1}, H. Heron¹³, J. Hewett⁴, A. Hime⁶, M. Howe¹⁵, J.G. Hykawy⁴, M.C.P. Isaac⁵, P. Jagam¹², N.A. Jelley¹³, C. Jillings⁹, G. Jonkmans^{4,1}, J. Karn¹², P.T. Keener¹⁴, K. Kirch⁶, J.R. Klein¹⁴, A.B. Knox¹³, R.J. Komar^{10,9}, R. Kouzes⁸, T. Kutter¹⁰, C.C.M. Kyba¹⁴, J. Law¹², I.T. Lawson¹², M. Lay¹³, H.W. Lee⁹, K.T. Lesko⁵, J.R. Leslie⁹, I. Levine³, W. Locke¹³, M.M. Lowry⁸, S. Luoma⁴, J. Lyon¹³, S. Majerus¹³, H.B. Mak⁹, A.D. Marino⁵, N. McCauley¹³, A.B. McDonald^{9,8}, D.S. McDonald¹⁴, K. McFarlane³, G. McGregor¹³, W. McLatchie⁹, R. Meijer Drees¹⁵, H. Mes³, C. Miffin³, G.G. Miller⁶, G. Milton¹, B.A. Moffat⁹, M. Moorhead^{13,5}, C.W. Nally¹⁰, M.S. Neubauer¹⁴, F.M. Newcomer¹⁴, H.S. Ng¹⁰, A.J. Noble^{3†}, E.B. Norman⁵, V.M. Novikov³, M. O'Neill³, C.E. Okada⁵, R.W. Ollerhead¹², M. Omori¹³, J.L. Orrell¹⁵, S.M. Oser¹⁴, A.W.P. Poon^{5,6,10,15}, T.J. Radcliffe⁹, A. Roberge⁴, B.C. Robertson⁹, R.G.H. Robertson^{15,6}, J.K. Rowley², V.L. Rusu¹⁴, E. Saettler⁴, K.K. Schaffer¹⁵, A. Schuelke⁵, M.H. Schwendener⁴, H. Seifert^{4,6,15}, M. Shatkey³, J.J. Simpson¹², D. Sinclair³, P. Skensved⁹, A.R. Smith⁵, M.W.E. Smith¹⁵, N. Starinsky³, T.D. Steiger¹⁵, R.G. Stokstad⁵, R.S. Storey^{7*}, B. Sur^{1,9}, R. Tafirout⁴, N. Tagg¹², N.W. Tanner¹³, R.K. Taplin¹³, M. Thorman¹³, P. Thornewell^{6,13,15}, P.T. Trent^{13†}, Y.I. Tserkovnyak¹⁰, R. Van Berg¹⁴, R.G. Van de Water^{14,6}, C.J. Virtue⁴, C.E. Waltham¹⁰, J.-X. Wang¹², D.L. Wark^{13,6§}, N. West¹³, J.B. Wilhelm⁶, J.F. Wilkerson^{15,6}, J. Wilson¹³, P. Wittich¹⁴, J.M. Wouters⁶, M. Yeh²

(The SNO Collaboration)

¹ Atomic Energy of Canada Limited, Chalk River Laboratories, Chalk River, Ontario K0J 1J0

² Chemistry Department, Brookhaven National Laboratory, Upton, NY 11973-5000

³ Carleton University, Ottawa, Ontario K1S 5B6 Canada

⁴ Department of Physics and Astronomy, Laurentian University, Sudbury, Ontario P3E 2C6 Canada

⁵ Institute for Nuclear and Particle Astrophysics and Nuclear Science Division, Lawrence Berkeley National Laboratory, Berkeley, CA 94720

⁶ Los Alamos National Laboratory, Los Alamos, NM 87545

⁷ National Research Council of Canada, Ottawa, Ontario K1A 0R6 Canada

⁸ Department of Physics, Princeton University, Princeton, NJ 08544

⁹ Department of Physics, Queen's University, Kingston, Ontario K7L 3N6 Canada

¹⁰ Department of Physics and Astronomy, University of British Columbia, Vancouver, BC V6T 1Z1 Canada

¹¹ Department of Physics, University of California, Irvine, CA 92717

¹² Physics Department, University of Guelph, Guelph, Ontario N1G 2W1 Canada

¹³ Nuclear and Astrophysics Laboratory, University of Oxford, Keble Road, Oxford, OX1 3RH, UK

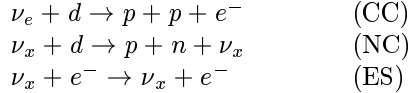
¹⁴ Department of Physics and Astronomy, University of Pennsylvania, Philadelphia, PA 19104-6396,

¹⁵ Center for Experimental Nuclear Physics and Astrophysics, and Department of Physics, University of Washington, Seattle, WA 98195

(30 June 2001)

Solar neutrinos from the decay of ^8B have been detected at the Sudbury Neutrino Observatory (SNO) via the charged current (CC) reaction on deuterium and by the elastic scattering (ES) of electrons. The CC reaction is sensitive exclusively to ν_e 's, while the ES reaction also has a small sensitivity to ν_μ 's and ν_τ 's. The flux of ν_e 's from ^8B decay measured by the CC reaction rate is $\phi^{\text{CC}}(\nu_e) = 1.75 \pm 0.07$ (stat.) $_{-0.11}^{+0.12}$ (sys.) ± 0.05 (theor.) $\times 10^6 \text{ cm}^{-2}\text{s}^{-1}$. Assuming no flavor transformation, the flux inferred from the ES reaction rate is $\phi^{\text{ES}}(\nu_x) = 2.39 \pm 0.34$ (stat.) $_{-0.14}^{+0.16}$ (sys.) $\times 10^6 \text{ cm}^{-2}\text{s}^{-1}$. Comparison of $\phi^{\text{CC}}(\nu_e)$ to the Super-Kamiokande Collaboration's precision value of $\phi^{\text{ES}}(\nu_x)$ yields a 3.3σ difference, assuming the systematic uncertainties are normally distributed, providing evidence that there is a non-electron flavor active neutrino component in the solar flux. The total flux of active ^8B neutrinos is thus determined to be $5.44 \pm 0.99 \times 10^6 \text{ cm}^{-2}\text{s}^{-1}$, in close agreement with the predictions of solar models.

Solar neutrino experiments over the past 30 years [1–6] have measured fewer neutrinos than are predicted by models of the Sun [7,8]. One explanation for the deficit is the transformation of the Sun’s electron-type neutrinos into other active flavors. The Sudbury Neutrino Observatory (SNO) measures the ^8B solar neutrinos through the reactions:



The charged current reaction (CC) is sensitive exclusively to electron-type neutrinos, while the neutral current (NC) is sensitive to all active neutrino flavors ($x = e, \mu, \tau$). The elastic scattering (ES) reaction is sensitive to all flavors as well, but with reduced sensitivity to ν_μ and ν_τ . By itself, the ES reaction cannot provide a measure of the total ^8B flux or its flavor content. Comparison of the ^8B flux deduced from the ES reaction assuming no neutrino oscillations ($\phi^{\text{ES}}(\nu_x)$), to that measured by the CC reaction ($\phi^{\text{CC}}(\nu_e)$) can provide clear evidence of flavor transformation without reference to solar model flux calculations. If neutrinos from the Sun change into other active flavors, then $\phi^{\text{CC}}(\nu_e) < \phi^{\text{ES}}(\nu_x)$.

This Letter presents the first results from SNO on the ES and CC reactions. SNO’s measurement of $\phi^{\text{ES}}(\nu_x)$ is consistent with previous measurements described in Ref [5]. The measurement of $\phi^{\text{CC}}(\nu_e)$, however, is significantly smaller and is therefore inconsistent with the null hypothesis that all observed solar neutrinos are ν_e . A measurement using the NC reaction, which has equal sensitivity to all neutrino flavors, will be reported in a future publication.

SNO [9] is an imaging water Čerenkov detector located at a depth of 6010 m of water equivalent in the INCO, Ltd. Creighton mine near Sudbury, Ontario. It features 1000 metric tons of ultra-pure D_2O contained in a 12 m diameter spherical acrylic vessel. This sphere is surrounded by a shield of ultra-pure H_2O contained in a 34 m high barrel-shaped cavity of maximum diameter 22 m. A stainless steel structure 17.8 m in diameter supports 9456 20-cm photomultiplier tubes (PMTs) with light concentrators. Approximately 55% of the light produced within 7 m of the center of the detector will strike a PMT.

The data reported here were recorded between Nov. 2, 1999 and Jan. 15, 2001 and correspond to a live time of 240.95 days. Events are defined by a multiplicity trigger of 18 or more PMTs exceeding a threshold of ~ 0.25 photo-electrons within a time window of 93 ns. The trigger reaches 100% efficiency at 23 PMTs. The total instantaneous trigger rate is 15-18 Hz, of which 6-8 Hz is the data trigger. For every event trigger, the time and charge responses of each participating PMT are recorded.

The data were partitioned into two sets, with approximately 70% used to establish the data analysis proce-

TABLE I. Data reduction steps.

Analysis step	Number of events
Total event triggers	355 320 964
Neutrino data triggers	143 756 178
$N_{\text{hit}} \geq 30$	6 372 899
Instrumental background cuts	1 842 491
Muon followers	1 809 979
High level cuts ^a	923 717
Fiducial volume cut	17 884
Threshold cut	1 169
Total events	1 169

^aReconstruction figures of merit, prompt light, and $\langle \theta_{ij} \rangle$.

dures and 30% reserved for a blind test of statistical bias in the analysis. The analysis procedures were frozen before the blind data set was analyzed, and no statistically significant differences in the data sets were found. We present here the analysis of the combined data sets.

Calibration of the PMT time and charge pedestals, slopes, offsets, charge vs. time dependencies, and second order rate dependencies are performed using electronic pulsers and pulsed light sources. Optical calibration is obtained using a diffuse source of pulsed laser light at 337, 365, 386, 420, 500 and 620 nm. The absolute energy scale and uncertainties are established with a triggered ^{16}N source (predominantly 6.13-MeV γ 's) deployed over two planar grids within the D_2O and a linear grid in the H_2O . The resulting Monte Carlo predictions of detector response are tested using a ^{252}Cf neutron source, which provides an extended distribution of 6.25-MeV γ rays from neutron capture, and a $^3\text{H}(p, \gamma)^4\text{He}$ [10] source providing 19.8-MeV γ rays. The volume-weighted mean response is approximately nine PMT hits per MeV of electron energy.

Table I details the steps in data reduction. The first of these is the elimination of instrumental backgrounds. Electrical pickup may produce false PMT hits, while electrical discharges in the PMTs or insulating detector materials produce light. These backgrounds have characteristics very different from Čerenkov light, and are eliminated using cuts based only on the PMT positions, the PMT time and charge data, event-to-event time correlations, and veto PMTs. This step in the data reduction is verified by comparing results from two independent background rejection analyses.

For events passing the first stage, the calibrated times and positions of the hit PMTs are used to reconstruct the vertex position and the direction of the particle. The reconstruction accuracy and resolution are measured using Compton electrons from the ^{16}N source, and the energy and source variation of reconstruction are checked with a ^8Li β source. Angular resolution is measured using Compton electrons produced more than 150 cm from the ^{16}N source. At these energies, the vertex resolution is 16 cm and the angular resolution is 26.7 degrees.

An effective kinetic energy, T_{eff} , is assigned to each event passing the reconstruction stage. T_{eff} is calculated using prompt (unscattered) Čerenkov photons and the position and direction of the event. The derived energy response of the detector can be characterized by a Gaussian:

$$R(E_{\text{eff}}, E_e) = \frac{1}{\sqrt{2\pi}\sigma_E(E_e)} \exp\left[-\frac{1}{2}\left(\frac{E_{\text{eff}} - E_e}{\sigma_E(E_e)}\right)^2\right]$$

where E_e is the total electron energy, $E_{\text{eff}} = T_{\text{eff}} + m_{e^+}$, and $\sigma_E(E_e) = (-0.4620 + 0.5470\sqrt{E_e} + 0.008722E_e)$ MeV is the energy resolution. The uncertainty on the energy scale is found to be $\pm 1.4\%$, which results in a flux uncertainty nearly 4 times larger. For validation, a second energy estimator counts all PMTs hit in each event, N_{hit} , without position and direction corrections.

Further instrumental background rejection is obtained using reconstruction figures of merit, PMT time residuals, and the average angle between hit PMTs ($\langle\langle\theta_{ij}\rangle\rangle$), measured from the reconstructed vertex. These cuts test the hypothesis that each event has the characteristics of single electron Čerenkov light. The effects of these and the rest of the instrumental background removal cuts on neutrino signals are quantified using the ^8Li and ^{16}N sources deployed throughout the detector. The volume-weighted neutrino signal loss is measured to be $1.4^{+0.7}_{-0.6}\%$ and the residual instrumental contamination for the data set within the $\text{D}_{2\text{O}}$ is $< 0.2\%$. Lastly, cosmic ray induced neutrons and spallation products are removed using a 20 s coincidence window with the parent muon.

Figure 1 shows the radial distribution of all remaining events above a threshold of $T_{\text{eff}} \geq 6.75$ MeV. The distribution is expressed as a function of the volume-weighted radial variable $(R/R_{\text{AV}})^3$, where $R_{\text{AV}} = 6.00$ m is the radius of the acrylic vessel. Above this energy threshold, there are contributions from CC events in the $\text{D}_{2\text{O}}$, ES events in the $\text{D}_{2\text{O}}$ and H_2O , a residual tail of neutron capture events, and high energy γ rays from radioactivity in the outer detector. The data show a clear signal within the $\text{D}_{2\text{O}}$ volume. For $(R/R_{\text{AV}})^3 > 1.0$ the distribution rises into the H_2O region until it is cut off by the acceptance of the PMT light collectors at $R \sim 7.0$ m. A fiducial volume cut is applied at $R = 5.50$ m to reduce backgrounds from regions exterior to the $\text{D}_{2\text{O}}$, and to minimize systematic uncertainties associated with optics and reconstruction near the acrylic vessel.

Possible backgrounds from radioactivity in the $\text{D}_{2\text{O}}$ and H_2O are measured by regular low level radio-assays of U and Th decay chain products in these regions. The Čerenkov light character of $\text{D}_{2\text{O}}$ and H_2O radioactivity backgrounds is used *in situ* to monitor backgrounds between radio-assays. Low energy radioactivity backgrounds are removed by the high threshold imposed, as are most neutron capture events. Monte Carlo calculations predict that the H_2O shield effectively reduces contributions of low energy (< 4 MeV) γ rays from the PMT

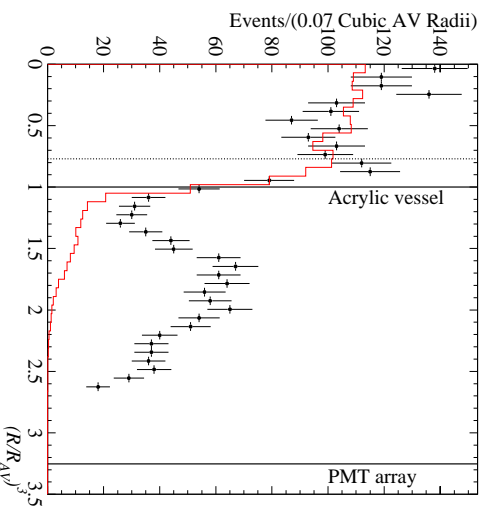


FIG. 1. Distribution of event candidates with $T_{\text{eff}} \geq 6.75$ MeV as a function of the volume weighted radial variable $(R/R_{\text{AV}})^3$. The Monte Carlo simulation of the signals, weighted by the results from the signal extraction, is shown as a histogram. The dotted line indicates the fiducial volume cut used in this analysis.

array, and these predictions are verified by deploying an encapsulated Th source in the vicinity of the PMT support sphere. High energy γ rays from the cavity are also attenuated by the H_2O shield. A limit on their leakage into the fiducial volume is estimated by deploying the ^{16}N source near the edge of the detector's active volume. The total contribution from all radioactivity in the detector is found to be $< 0.2\%$ for low energy backgrounds and $< 0.8\%$ for high energy backgrounds.

The final data set contains 1169 events after the fiducial volume and kinetic energy threshold cuts. Figure 2 (a) displays the distribution of $\cos\theta_{\odot}$, the angle between the reconstructed direction of the event and the instantaneous direction from the Sun to the Earth. The forward peak in this distribution arises from the kinematics of the ES reaction, while CC electrons are expected to have a distribution which is $(1 - 0.340\cos\theta_{\odot})$ [11], before accounting for detector response.

The data are resolved into contributions from CC, ES, and neutron events above threshold using probability density functions (pdfs) in T_{eff} , $\cos\theta_{\odot}$, and $(R/R_{\text{AV}})^3$, generated from Monte Carlo simulations assuming no flavor transformation and the shape of the standard ^8B spectrum [12] (*hep* neutrinos are not included in the fit). The extended maximum likelihood method used in the signal extraction yields 975.4 ± 39.7 CC events, 106.1 ± 15.2 ES events, and 87.5 ± 24.7 neutron events for the fiducial volume and the threshold chosen, where the uncertainties given are statistical only. The dominant

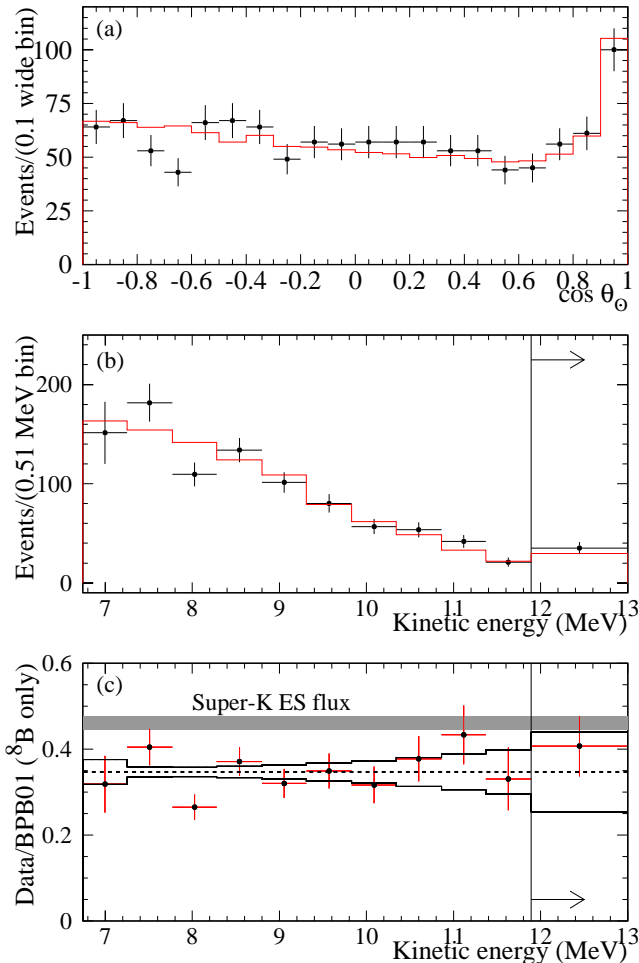


FIG. 2. Distributions of (a) $\cos \theta_\odot$, and (b) extracted kinetic energy spectrum for CC events with $R \leq 5.50$ m and $T_{\text{eff}} \geq 6.75$ MeV. The Monte Carlo simulations for an undistorted ^8B spectrum are shown as histograms. The ratio of the data to the expected kinetic energy distribution with correlated systematic errors is shown in (c). The uncertainties in the ^8B spectrum [12] have not been included.

sources of systematic uncertainty in this signal extraction are the energy scale uncertainty and reconstruction accuracy, as shown in Table II. The CC and ES signal decomposition gives consistent results when used with the N_{hit} energy estimator, as well as with different choices of the analysis threshold and the fiducial volume up to 6.20 m with backgrounds characterized by pdfs.

The CC spectrum can be extracted from the data by removing the constraint on the shape of the CC pdf and repeating the signal extraction.

Figure 2 (b) shows the kinetic energy spectrum with statistical error bars, with the ^8B spectrum of Ortiz *et al.* [12] scaled to the data. The ratio of the data to the prediction [7] is shown in Figure 2 (c). The bands represent the 1σ uncertainties derived from the most significant energy-dependent systematic errors. There is no

TABLE II. Systematic error on fluxes.

Error source	CC error (percent)	ES error (per cent)
Energy scale	-5.2, +6.1	-3.5, +5.4
Energy resolution	± 0.5	± 0.3
Energy scale non-linearity	± 0.5	± 0.4
Vertex accuracy	± 3.1	± 3.3
Vertex resolution	± 0.7	± 0.4
Angular resolution	± 0.5	± 2.2
High energy γ 's	-0.8, +0.0	-1.9, +0.0
Low energy background	-0.2, +0.0	-0.2, +0.0
Instrumental background	-0.2, +0.0	-0.6, +0.0
Trigger efficiency	0.0	0.0
Live time	± 0.1	± 0.1
Cut acceptance	-0.6, +0.7	-0.6, +0.7
Earth orbit eccentricity	± 0.1	± 0.1
^{17}O , ^{18}O	0.0	0.0
Experimental uncertainty	-6.2, +7.0	-5.7, +6.8
Cross section	3.0	0.5
Solar Model	-16, +20	-16, +20

evidence for a deviation of the spectral shape from the predicted shape under the non-oscillation hypothesis.

Normalized to the integrated rates above the kinetic energy threshold of $T_{\text{eff}} = 6.75$ MeV, the measured ^8B neutrino fluxes assuming the standard spectrum shape [12] are:

$$\phi_{\text{SNO}}^{\text{CC}}(\nu_e) = 1.75 \pm 0.07 \text{ (stat.)}_{-0.11}^{+0.12} \text{ (sys.)} \pm 0.05 \text{ (theor.)} \\ \times 10^6 \text{ cm}^{-2}\text{s}^{-1}$$

$$\phi_{\text{SNO}}^{\text{ES}}(\nu_x) = 2.39 \pm 0.34 \text{ (stat.)}_{-0.14}^{+0.16} \text{ (sys.)} \times 10^6 \text{ cm}^{-2}\text{s}^{-1}$$

where the theoretical uncertainty is the CC cross section uncertainty [13]. Radiative corrections have not been applied to the CC cross section, but they are expected to decrease the measured $\phi^{\text{CC}}(\nu_e)$ flux [14] by up to a few percent. The difference between the ^8B flux deduced from the ES rate and that deduced from the CC rate in SNO is $0.64 \pm 0.40 \times 10^6 \text{ cm}^{-2}\text{s}^{-1}$, or 1.6σ . SNO's ES rate measurement is consistent with the precision measurement by the Super-Kamiokande Collaboration of the ^8B flux using the same ES reaction [5]:

$$\phi_{\text{SK}}^{\text{ES}}(\nu_x) = 2.32 \pm 0.03 \text{ (stat.)}_{-0.07}^{+0.08} \text{ (sys.)} \times 10^6 \text{ cm}^{-2}\text{s}^{-1}.$$

The difference between the flux $\phi^{\text{ES}}(\nu_x)$ measured by Super-Kamiokande via the ES reaction and the $\phi^{\text{CC}}(\nu_e)$ flux measured by SNO via the CC reaction is $0.57 \pm 0.17 \times 10^6 \text{ cm}^{-2}\text{s}^{-1}$, or 3.3σ [15], assuming that the systematic errors are normally distributed. The probability that a downward fluctuation of the Super-Kamiokande result would produce a SNO result $\geq 3.3\sigma$ is 0.04%. For reference, the ratio of the SNO CC ^8B flux to that of the BPB01 solar model [7] is 0.347 ± 0.029 , where all uncertainties are added in quadrature.

If oscillation solely to a sterile neutrino is occurring, the SNO CC-derived ^8B flux above a threshold of

6.75 MeV will be consistent with the integrated Super-Kamiokande ES-derived ${}^8\text{B}$ flux above a threshold of 8.5 MeV [16]. Adjusting the ES threshold [5] this derived flux difference is $0.53 \pm 0.17 \times 10^6 \text{ cm}^{-2}\text{s}^{-1}$, or 3.1σ . The probability of a downward fluctuation $\geq 3.1\sigma$ is 0.13%. These data are therefore evidence of a non-electron active flavor component in the solar neutrino flux. These data are also inconsistent with the “Just-So²” parameters for neutrino oscillation [18].

Figure 3 displays the inferred flux of non-electron flavor active neutrinos ($\phi(\nu_{\mu\tau})$) against the flux of electron neutrinos. The two data bands represent the one standard deviation measurements of the SNO CC rate and the Super-Kamiokande ES rate. The error ellipses represent the 68%, 95%, and 99% joint probability contours for $\phi(\nu_e)$ and $\phi(\nu_{\mu\tau})$. The best fit to $\phi(\nu_{\mu\tau})$ is:

$$\phi(\nu_{\mu\tau}) = 3.69 \pm 1.13 \times 10^6 \text{ cm}^{-2}\text{s}^{-1}.$$

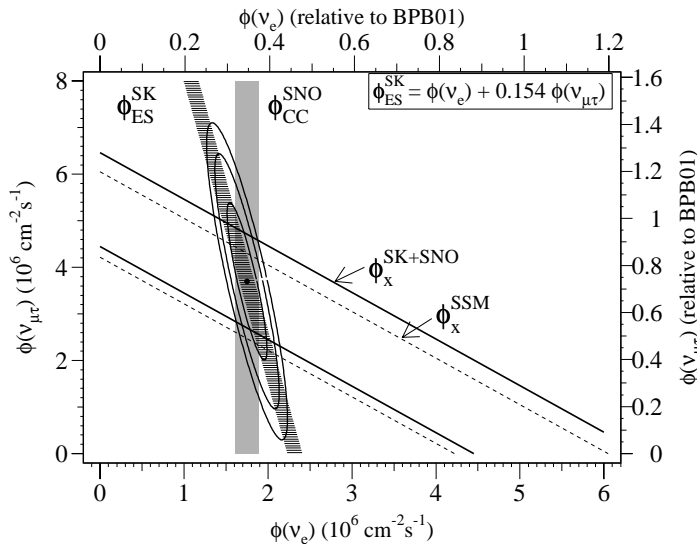


FIG. 3. Flux of ${}^8\text{B}$ solar neutrinos which are μ or τ flavor vs. the flux of electron neutrinos as deduced from the SNO and Super-Kamiokande data. The diagonal bands show the total ${}^8\text{B}$ flux $\phi(\nu_x)$ as predicted by BPB01 (dashed lines) and that derived from the SNO and Super-Kamiokande measurements (solid lines). The intercepts of these bands with the axes represent the $\pm 1\sigma$ errors.

The total flux of active ${}^8\text{B}$ neutrinos is determined to be:

$$\phi(\nu_x) = 5.44 \pm 0.99 \times 10^6 \text{ cm}^{-2}\text{s}^{-1}.$$

This result is displayed as a diagonal band in Fig. 3, and is in excellent agreement with predictions of standard solar models [7,8].

Assuming that the oscillation of massive neutrinos explains both the evidence for electron neutrino flavor change presented here and the atmospheric neutrino data of the Super-Kamiokande collaboration [19], two separate splittings of the squares of the neutrino mass eigenvalues are indicated: $< 10^{-3} \text{ eV}^2$ for the solar sector [17,18] and $\simeq 3.5 \times 10^{-3} \text{ eV}^2$ for atmospheric neutrinos. These results, together with the beta spectrum of tritium [22], limit the sum of mass eigenvalues of active neutrinos to be between 0.05 and 8.4 eV, corresponding to a constraint of $0.001 < \Omega_\nu < 0.18$ for the contribution to the critical density of the Universe [20,21].

In summary, the results presented here are the first direct indication of a non-electron flavor component in the solar neutrino flux, and enable the first determination of the total flux of ${}^8\text{B}$ neutrinos generated by the Sun.

This research was supported by the Natural Sciences and Engineering Research Council of Canada, Industry Canada, National Research Council of Canada, Northern Ontario Heritage Fund Corporation and the Province of Ontario, the United States Department of Energy, and in the United Kingdom by the Science and Engineering Research Council and the Particle Physics and Astronomy Research Council. Further support was provided by INCO, Ltd., Atomic Energy of Canada Limited (AECL), Agra-Monenco, Canatom, Canadian Microelectronics Corporation, AT&T Microelectronics, Northern Telecom and British Nuclear Fuels, Ltd. The heavy water was loaned by AECL with the cooperation of Ontario Power Generation.

* Deceased.

† Permanent address: TRIUMF, 4004 Wesbrook Mall, Vancouver, BC V6T 2A3, Canada.

‡ Permanent address: Birkbeck College, University of London, Malet Road, London WC1E 7HX, UK.

§ Permanent address: Rutherford Appleton Laboratory, Chilton, Didcot, Oxon, OX11 0QX, and University of Sussex, Physics and Astronomy Department, Brighton BN1 9QH, UK.

- [1] B.T. Cleveland *et al.*, *Astrophys. J.* **496**, 505 (1998).
- [2] K.S. Hirata *et al.*, *Phys. Rev. Lett.* **65**, 1297 (1990); K.S. Hirata *et al.*, *Phys. Rev. D* **44**, 2241 (1991), **45** 2170E (1992); Y. Fukuda *et al.*, *Phys. Rev. Lett.* **77**, 1683 (1996).
- [3] J.N. Abdurashitov *et al.*, *Phys. Rev. C* **60**, 055801, (1999).
- [4] W. Hampel *et al.*, *Phys. Lett. B* **447**, 127 (1999).
- [5] S. Fukuda *et al.*, *Phys. Rev. Lett.* **86**, 5651 (2001).
- [6] M. Altmann *et al.*, *Phys. Lett. B* **490**, 16 (2000).
- [7] J.N. Bahcall, M. H. Pinsonneault, and S. Basu, *astro-ph/0010346 v2*. The reference ${}^8\text{B}$ neutrino flux is $5.05 \times 10^6 \text{ cm}^{-2}\text{s}^{-1}$.

- [8] A.S. Brun, S. Turck-Chièze, and J.P. Zahn, *Astrophys. J.* **525**, 1032 (1999); S. Turck-Chièze *et al.*, *Ap. J. Lett.*, v. **555** July 1, 2001.
- [9] The SNO Collaboration, *Nucl. Instr. and Meth.* **A449**, 172 (2000).
- [10] A.W.P. Poon *et al.*, *Nucl. Instr. and Meth.* **A452**, 115, (2000).
- [11] J.F. Beacom and P. Vogel, hep-ph/9903554, *Phys. Rev. Lett.* **83**, 5222 (1999).
- [12] C.E. Ortiz *et al.*, *Phys. Rev. Lett.* **85**, 2909 (2000).
- [13] S. Nakamura, T. Sato, V. Gudkov, and K. Kubodera, *Phys. Rev. C* **63**, 034617 (2001); M. Butler, J.-W. Chen, and X. Kong, *Phys. Rev. C* **63**, 035501 (2001); G. 't Hooft, *Phys. Lett.* **37B** 195 (1971). The Butler *et al.* cross section with $L_{I,A} = 5.6 \text{ fm}^3$ is used.
- [14] I. S. Towner, J. Beacom, and S. Parke, private communication; I. S. Towner, *Phys. Rev. C* **58** 1288 (1998), J. Beacom and S. Parke, hep-ph/0106128; J.N. Bahcall, M. Kamionkowski, and A. Sirlin, *Phys. Rev. D* **51** 6146 (1995).
- [15] Given the limit set for the *hep* flux by Ref. [5], the effects of the *hep* contribution may increase this difference by a few percent.
- [16] G. L. Fogli, E. Lisi, A. Palazzo, and F.L. Villante *Phys. Rev. D* **63**, 113016 (2001); F.L. Villante, G. Fiorentini and E. Lisi *Phys. Rev. D* **59** 013006 (1999).
- [17] M. Apollonio *et al.*, *Phys. Lett. B* **466**, 415 (1999).
- [18] J.N. Bahcall, P.I. Krastev, and A.Yu. Smirnov, *JHEP* **05**, 015 (2001).
- [19] T. Toshito *et al.* hep-ex/0105023
- [20] Allen's *Astrophysical Quantities*, 4th ed., ed. Arthur Cox, (New York:Springer-Verlag), 2000. *European Physical Journal* **C15**, 1 (2000)
- [21] H. Pas and T. J. Weiler, *Phys. Rev. D* **63**, 113015 (2001).
- [22] J. Bonn *et al.* *Nucl. Phys. Proc. B Suppl.* **91**, 273 (2001).